

Cite this: *J. Mater. Chem. A*, 2017, 5, 18214

P2-type transition metal oxides for high performance Na-ion battery cathodes†

Chao Luo, Alex Langrock, Xiulin Fan, Yujia Liang  and Chunsheng Wang *

The particle pulverization induced by volume change and the disproportionation reaction of Mn^{3+} to Mn^{4+} and electrolyte-soluble Mn^{2+} are two major challenges for $\text{Na}_{0.67}\text{MnO}_2$ cathodes in Na-ion batteries. Herein, Ni and/or Fe doped $\text{Na}_{0.67}\text{MnO}_2$ was synthesized to suppress the particle pulverization and disproportionation reaction. The replacement of 33% Mn ions by Ni in $\text{Na}_{0.67}\text{MnO}_2$ can effectively reduce the particle pulverization and disproportionation of Mn^{3+} , resulting in improved cycling stability at the cost of reduced capacity. To develop a high capacity and long cycle life cathode material, Ni in $\text{Na}_{0.67}\text{Ni}_{0.33}\text{Mn}_{0.67}\text{O}_2$ is further partially substituted by Fe to generate $\text{Na}_{0.67}\text{Fe}_{0.20}\text{Ni}_{0.15}\text{Mn}_{0.65}\text{O}_2$, which retains ~70% of its initial capacity after 900 cycles, corresponding to a very low capacity decay rate of 0.033% per cycle. To the best of our knowledge, the $\text{Na}_{0.67}\text{Fe}_{0.20}\text{Ni}_{0.15}\text{Mn}_{0.65}\text{O}_2$ synthesized by ultrasonic spray pyrolysis (USP) represents one of the best cathode materials for Na-ion batteries to date. In addition, a thin layer (5 nm) of Al_2O_3 is deposited on the $\text{Na}_{0.67}\text{MnO}_2$ electrode by atomic layer deposition (ALD) to further reduce the dissolution of Mn ions and accommodate the volume change, which further extend the cycling stability of $\text{Na}_{0.67}\text{MnO}_2$ electrodes.

Received 24th May 2017

Accepted 31st July 2017

DOI: 10.1039/c7ta04515h

rsc.li/materials-a

Introduction

Lithium ion batteries, which play a dominant role in portable electronics, are promising energy storage devices for electric vehicles and smart grids. As the demand for lithium rises, the unevenly distributed and limited lithium resources become a bottleneck for the large-scale application of Li-ion batteries.^{1,2} It is pivotal to find an appropriate substitution for lithium in rechargeable batteries. To date, sodium, which shares similar chemistry with lithium, is considered as a promising candidate for next generation rechargeable batteries due to its low cost and abundance.^{3–5}

Considerable research efforts have been devoted to developing high performance anode and cathode materials for Na-ion batteries. Porous carbon,⁶ metal sulfides,^{7–9} phosphorous,^{10,11} and alloys^{12,13} have all been investigated as anode materials for Na-ion batteries. Great success in high capacity and long cycle life anodes requires comparable cathodes to achieve high performance Na-ion batteries. However, the electrochemical performance of cathode materials such as O3-type and P2-type sodium metal oxides,^{14–21} sodium metal phosphates,^{22–24} sodium metal sulfates,²⁵ selenium,^{26,27} and sulfur^{28,29} still cannot satisfy the high requirements for industrial application. It is of great significance to develop high performance

cathode materials for Na-ion batteries.^{30–34} Among the large variety of cathode materials, Na_xMnO_2 ($0 < x \leq 1$) phases are promising due to the low cost of precursors and simple synthetic routes.³⁵ In these compounds, alkali metals are coordinated to six oxygen atoms in either a trigonal prismatic (P) or octahedral geometry (O). Additional numbers are included in the nomenclature of these layered compounds to discern the alkali metal layers. For example, P2 denotes that the environment is prismatic and the unit cell is comprised of two MnO_2 sheets. The P2 phase has shown the most promising performance among the various Na_xMnO_2 phases.³⁶ However, particle pulverization and the disproportionation reaction of Mn^{3+} to Mn^{4+} and electrolyte-soluble Mn^{2+} are two crucial factors responsible for the structural instability of Na_xMnO_2 .³⁷ To alleviate particle pulverization and dissolution of Mn^{2+} , foreign metallic ions are introduced to decrease the Mn^{3+} content and stabilize the crystal structure. Element doping in Na_xMnO_2 was selected to suppress the dissolution of Mn^{2+} .^{38–42} Yabuuchi *et al.* were the first to report the electrochemical sodium insertion reaction of P2- and O3-type Fe doped $\text{Na}_x[\text{Fe}_{0.5}\text{Mn}_{0.5}]\text{O}_2$.³⁸ B. Mortemard de Boisse *et al.* also studied the electrochemical performance of P2- and O3- $\text{Na}_x\text{Mn}_{1-y}\text{Fe}_y\text{O}_2$ with varying stoichiometries of Na, Fe, and Mn.⁴³ Both studies showed that P2-type oxides have higher reversible capacity than the O3-type, but cycling stability improvement is needed.

In this paper, three P2-type layered sodium metal oxides, $\text{Na}_{0.67}\text{MnO}_2$, $\text{Na}_{0.67}\text{Ni}_{0.33}\text{Mn}_{0.67}\text{O}_2$ and $\text{Na}_{0.67}\text{Fe}_{0.20}\text{Ni}_{0.15}\text{Mn}_{0.65}\text{O}_2$, are synthesized by ultrasonic spray pyrolysis (USP) followed by high temperature annealing. The P2-type $\text{Na}_{0.67}\text{MnO}_2$

Department of Chemical and Biomolecular Engineering, University of Maryland, College Park, MD 20742, USA. E-mail: cswang@umd.edu

† Electronic supplementary information (ESI) available. See DOI: 10.1039/c7ta04515h

delivers a reversible capacity of 176 mA h g⁻¹ at 0.1C (1C = 244 mA g⁻¹) in a narrow cutoff window from 2.0 V to 3.8 V, and a reversible capacity of 205 mA h g⁻¹ at 0.1C in an expanded voltage window from 1.5 V to 4.3 V. To mitigate the disproportionation of Mn³⁺, 33% Mn in Na_{0.67}MnO₂ is replaced by Ni, and the formed P2-type Na_{0.67}Ni_{0.33}Mn_{0.67}O₂ exhibits good cycling stability, but low reversible capacity (110 mA h g⁻¹ in a narrow cutoff window). To obtain a high capacity and long cycle life cathode material, Ni is further partially substituted by Fe to generate P2-type Na_{0.67}Fe_{0.20}Ni_{0.15}Mn_{0.65}O₂, which delivers a reversible capacity of 150 mA h g⁻¹ at 0.1C in a narrow cut-off window from 2.0 V to 3.8 V, and a reversible capacity of 250 mA h g⁻¹ at 0.1C in an expanded voltage window from 1.5 V to 4.3 V. Na_{0.67}Fe_{0.20}Ni_{0.15}Mn_{0.65}O₂ can retain its initial capacity in a narrow cut-off window at 1C for 350 cycles. To the best of our knowledge, the layered transition metal oxides synthesized by ultrasonic spray pyrolysis represent the best cathode materials for Na-ion batteries to date. To further improve the performance of Na_{0.67}MnO₂ in the expanded voltage window, an ALD method is employed to deposit a thin layer (5 nm) of Al₂O₃ on the Na_{0.67}MnO₂ electrode to accommodate the volume change and mitigate the dissolution of Mn²⁺ in the electrolyte. The Al₂O₃ coated Na_{0.67}MnO₂ electrode delivers an initial capacity of 150 mA h g⁻¹ at 0.1C, and retains a capacity of 129 mA h g⁻¹ after 100 cycles, corresponding to a slow capacity decay rate of 0.14% per cycle. The exceptional battery performance demonstrates that ALD is an effective method to increase the cycling stability of Na_{0.67}MnO₂ cathodes.

Experimental

Ultrasonic Spray Pyrolysis (USP) reactor system

The ultrasonic spray pyrolysis reactor system is composed of a precursor solution reservoir, an ultrasonic droplet generator (1.7 MHz), two tube furnaces in series, a quartz tube reactor (diameter 22/25 mm × 810 mm), and a filtration system for particle collection. Spray pyrolysis enables the production of spherical particles with compositional homogeneity with respect to the precursor solution. A frequency generator device is used to form ultrasonic vibrations, thereby creating fine aerosol droplets with a stoichiometric composition. The fine aerosol is transported *via* a carrier gas into a tubular furnace at a given temperature. Once in the furnace, the processes of diffusion, dehydration, and decomposition occur simultaneously to form nanoparticles of controlled size, morphology, and composition.

Materials synthesis

The synthesis of each material was carried out by mixing the stoichiometric amount of sodium nitrate and the corresponding metal nitrates in water. In each case, the total species precursor molar concentration was 0.08 M, and the spray pyrolysis temperature was 600 °C, while nitrogen carrier gas and quench gas flow rates were held constant at 3 lpm and 10 lpm, respectively. 600 °C was chosen as the optimum pyrolysis temperature, which corresponds to a residence time of

approximately 3 seconds. Particles were collected on a polytetrafluoroethylene (PTFE) filter using a brush. The as-prepared materials (Na_{0.67}MnO₂ and Na_{0.67}Fe_{0.20}Ni_{0.15}Mn_{0.65}O₂) were then annealed at 800 °C for 6 hours in air to obtain the desired phase. The as-prepared material (Na_{0.67}Ni_{0.33}Mn_{0.67}O₂) was then annealed at 950 °C for 6 hours in air to obtain the desired phase.

Atomic layer deposition

The electrodes were placed into an atomic layer deposition system (Beneq TFS 500) for Al₂O₃ deposition. High-purity nitrogen at 150 °C was used as the carrier gas for the whole process. To obtain the Al₂O₃ layer with a thickness of 5 nm, 50 precursor pulse cycles of ALD-Al₂O₃ were performed. Each cycle included alternating flows of trimethylaluminum (TMA, 4 s, Al precursor) and water (4 s, oxidant) separated by flows of pure nitrogen gas (4 and 10 s, respectively, carrier and cleaning gases). The thickness of the Al₂O₃ layer was about 1 Å for each precursor pulse cycle.

Materials characterization

Structural studies were performed by XRD on a D8 Advance with LynxEye and SolX (Bruker AXS, WI, USA) using CuKα radiation, scanning electron microscopy on a Hitachi (Tokyo, Japan) SU-70 HR-SEM with FFT images, and transmission electron microscopy on a JEOL 2100F field emission TEM (Tokyo, Japan).

Electrochemical measurements

Electrochemical performance was tested in a coin cell using sodium metal as the counter electrode and 1 M NaClO₄ in a mixture of fluoroethylene carbonate–dimethyl carbonate (FEC/DMC, 1 : 1 by volume) as the electrolyte and Celgard®3501 (Celgard LLC Corp., USA) as the separator. Cathodes consisted of 70 wt% active material, 20 wt% acetylene black, and 10 wt% sodium alginate, which were mixed with water and pasted on Al foil. The slurry coated on Al foil was punched into circular electrodes with an area mass loading of 1.5–2.0 mg cm⁻², and then dried at 100 °C in a vacuum. The charge/discharge behavior was tested using an ArbinBT2000 workstation (Arbin Instruments, TX, USA). Rate capability was examined by charging and discharging at different rates (1C = 260 mA g⁻¹). The cyclic voltammogram scanned at 0.1 mV s⁻¹ between 2.0 and 3.8 V was recorded using a Solatron 1260/1287 Electrochemical Interface (Solatron Metrology, UK).

Results and discussion

Three P2-type layered sodium metal oxides, Na_{0.67}MnO₂, Na_{0.67}Ni_{0.33}Mn_{0.67}O₂ and Na_{0.67}Fe_{0.20}Ni_{0.15}Mn_{0.65}O₂, are synthesized by USP followed by high temperature treatment. Fig. 1a shows the morphology of Na_{0.67}MnO₂ collected after USP. USP synthesized Na_{0.67}MnO₂ is micro-spheres with an average size of ~1 μm. After high temperature treatment in air, the microspheres become slabs with a depth of ~500 nm as shown in Fig. 1b. The distinct morphological change is triggered by the removal of carbonized sucrose and growth of

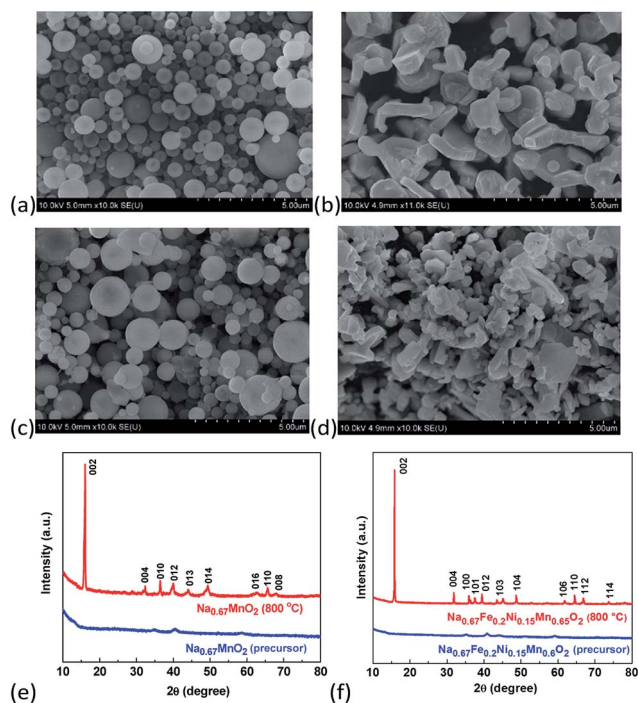


Fig. 1 SEM images of $\text{Na}_{0.67}\text{MnO}_2$ prepared by USP before (a) and after (b) heat treatment; SEM images of $\text{Na}_{0.67}\text{Fe}_{0.20}\text{Ni}_{0.15}\text{Mn}_{0.65}\text{O}_2$ prepared by USP before (c) and after (d) heat treatment; (e) XRD patterns of the $\text{Na}_{0.67}\text{MnO}_2$ sample before and after heat treatment; (f) XRD patterns of the $\text{Na}_{0.67}\text{Fe}_{0.20}\text{Ni}_{0.15}\text{Mn}_{0.65}\text{O}_2$ sample before and after heat treatment.

$\text{Na}_{0.67}\text{MnO}_2$ crystals. Similar phenomena were also observed for USP synthesized $\text{Na}_{0.67}\text{Ni}_{0.33}\text{Mn}_{0.67}\text{O}_2$ and $\text{Na}_{0.67}\text{Fe}_{0.20}\text{Ni}_{0.15}\text{Mn}_{0.65}\text{O}_2$, which also consist of micro-spherical particles with an average size of $\sim 1 \mu\text{m}$ (S1a† and Fig. 1c). After high temperature treatment in air, the morphology of $\text{Na}_{0.67}\text{Ni}_{0.33}\text{Mn}_{0.67}\text{O}_2$ becomes slabs (Fig. S1b†) with a depth of $\sim 1 \mu\text{m}$, while $\text{Na}_{0.67}\text{Fe}_{0.20}\text{Ni}_{0.15}\text{Mn}_{0.65}\text{O}_2$ turns out to be irregularly shaped micro-particles (Fig. 1d). The morphological difference among the three P2-type layered sodium metal oxides is probably due to the introduction of Fe and Ni, which alters the thermal properties and size of $\text{Na}_{0.67}\text{MnO}_2$ crystals.

To further characterize the structure of layered sodium metal oxides, transmission electron microscopy (TEM) and elemental mapping are performed. $\text{Na}_{0.67}\text{MnO}_2$ slabs are observed in Fig. S2,† which is consistent with the scanning electron microscopy (SEM) image in Fig. 1b. The elemental mapping in Fig. S2† displays that sodium, manganese and oxygen are uniformly distributed in the slab, demonstrating the uniform structure of $\text{Na}_{0.67}\text{MnO}_2$ crystals. The TEM image and elemental mapping results of $\text{Na}_{0.67}\text{Fe}_{0.20}\text{Ni}_{0.15}\text{Mn}_{0.65}\text{O}_2$ are shown in Fig. S3.† The $\text{Na}_{0.67}\text{Fe}_{0.20}\text{Ni}_{0.15}\text{Mn}_{0.65}\text{O}_2$ sample consists of irregularly shaped micro-particles, consistent with the SEM image in Fig. 1d. The elemental mapping demonstrates that sodium, iron, manganese, nickel and oxygen are uniformly distributed in the micro-particles, indicative of the uniform structure of $\text{Na}_{0.67}\text{Fe}_{0.20}\text{Ni}_{0.15}\text{Mn}_{0.65}\text{O}_2$ crystals. Therefore, SEM and TEM images show that three P2-type layered sodium metal oxides have different shapes but similar particle sizes.

The crystal structure of three P2-type layered sodium metal oxides are confirmed by XRD as shown in Fig. 1e, f and S4.† The precursors of $\text{Na}_{0.67}\text{MnO}_2$ and $\text{Na}_{0.67}\text{Fe}_{0.20}\text{Ni}_{0.15}\text{Mn}_{0.65}\text{O}_2$, prepared by USP without annealing, are amorphous structures, because the residence time ($\sim 3 \text{ s}$) during the USP process is too short to enable the growth of sodium metal oxide crystals. After high temperature treatment, the three sodium metal oxides display layered P2-type crystal structures as evidenced by the sharp peaks in XRD patterns. The strong and sharp XRD peak at 16 degree, corresponds to the typical 002 face for P2-type crystals. This peak can be observed in all three XRD patterns. The other XRD peaks for three sodium metal oxides can also be well-matched, demonstrating that the P2-type crystals of three sodium metal oxides are formed after high temperature treatment.

The electrochemical performance of three P2-type layered sodium metal oxides is measured in coin cells with the Na metal as the counter electrode. The sodiation/desodiation processes of the three sodium metal oxides are investigated by cyclic voltammetry in Fig. 2a, b and S5.† There are four pairs of broad peaks in Fig. 2a, corresponding to the stepwise intercalation/de-intercalation of sodium ions in the layered $\text{Na}_{0.67}\text{MnO}_2$ crystal. The anodic/cathodic peaks at 2.6/2.1 V correspond to the redox reaction of $\text{Mn}^{3+}/\text{Mn}^{4+}$.³⁶ After Ni is introduced in sodium metal

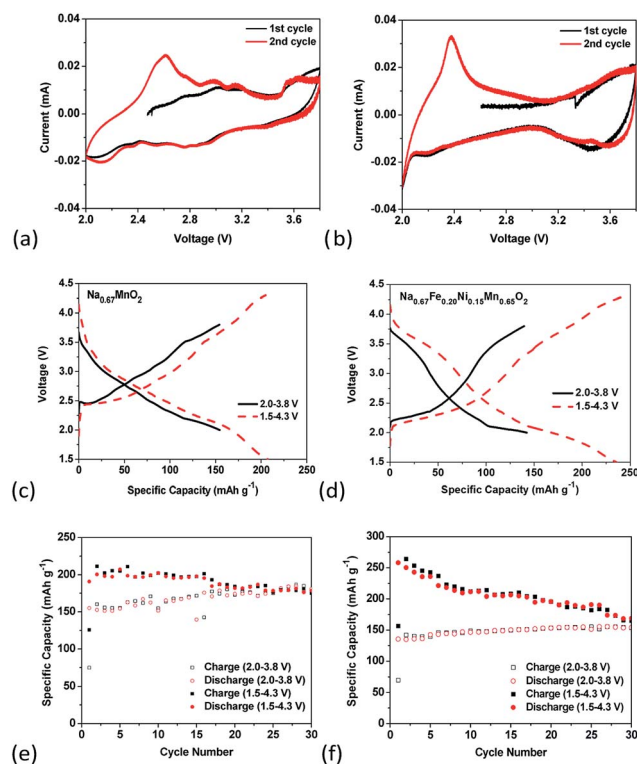


Fig. 2 Cyclic voltammograms of (a) $\text{Na}_{0.67}\text{MnO}_2$ and (b) $\text{Na}_{0.67}\text{Fe}_{0.20}\text{Ni}_{0.15}\text{Mn}_{0.65}\text{O}_2$ in the initial two cycles scanned between 2.0 and 3.8 V at a rate of 0.1 mV s^{-1} ; galvanostatic charge/discharge curves of $\text{Na}_{0.67}\text{MnO}_2$ (c) and $\text{Na}_{0.67}\text{Fe}_{0.20}\text{Ni}_{0.15}\text{Mn}_{0.65}\text{O}_2$ (d) cell cycled at a rate of 0.1C in the narrow and expanded voltage windows; capacity retention of $\text{Na}_{0.67}\text{MnO}_2$ (e) and $\text{Na}_{0.67}\text{Fe}_{0.20}\text{Ni}_{0.15}\text{Mn}_{0.65}\text{O}_2$ (f) cycled at a rate of 0.1C in the narrow and expanded voltage windows.

oxides, the four pairs of peaks become sharp (Fig. S5[†]). The sharp anodic/cathodic peaks at 3.7/3.6 V correspond to the redox reaction of Ni²⁺/Ni³⁺.³⁶ In Fig. 2b, only two pairs of anodic/cathodic peaks are observed in the Na_{0.67}Fe_{0.20}Ni_{0.15}Mn_{0.65}O₂ cathode. The sharp anodic/cathodic peaks at 2.4/2.0 V correspond to the redox reaction of Mn³⁺/Mn⁴⁺, while the broad anodic/cathodic peaks at 3.7/3.6 V correspond to the redox reaction of Ni²⁺/Ni³⁺. The completely different cyclic voltammograms for the three sodium metal oxides demonstrate that different phase transitions occur after iron and nickel doping in the Na_{0.67}MnO₂ cathode.

The charge/discharge behaviors of the three P2-type layered sodium metal oxides are evaluated in the narrow (2.0–3.8 V) and expanded voltage (1.5–4.3 V) windows at a current rate of 0.1C. As shown in Fig. 2c, the capacity of Na_{0.67}MnO₂ in the narrow (2.0–3.8 V) voltage window is 155 mA h g⁻¹, while the capacity in the expanded (1.5–4.3 V) voltage window is 205 mA h g⁻¹. After Ni doping (Fig. S7[†]), the capacity of Na_{0.67}Ni_{0.33}Mn_{0.67}O₂ in the narrow (2.0–3.8 V) voltage window decreases to 105 mA h g⁻¹, which is much lower than that of Na_{0.67}MnO₂, while the capacity in the expanded (2.0–4.5 V) voltage window is 158 mA h g⁻¹. The partial substitution of nickel by iron enhances the capacity. In Fig. 2d, Na_{0.67}Fe_{0.20}Ni_{0.15}Mn_{0.65}O₂ with iron and nickel doping delivers a reversible capacity of 145 mA h g⁻¹ in the narrow (2.0–3.8 V) voltage window, which is similar to Na_{0.67}MnO₂, while the capacity in the expanded (1.5–4.3 V) voltage window is 240 mA h g⁻¹. Both Na_{0.67}MnO₂ and Na_{0.67}Fe_{0.20}Ni_{0.15}Mn_{0.65}O₂ electrodes deliver lower desodiation capacity in the first charge than that in the following cycles as shown in Fig. S6,† due to high overpotential in the first charge induced by large strain/stress. Therefore, a very low charge current is needed in full cells to achieve high reversible capacity. Fig. 2e, f and S8[†] show the cycling stability of three P2-type layered sodium metal oxides in the narrow and expanded voltage windows. The P2-type layered sodium metal oxides suffer from rapid capacity fading in the expanded voltage window, while the capacity retention in the narrow voltage window is almost 100% after 25 cycles, demonstrating high cycling stability of P2-type layered sodium metal oxides in the narrow voltage window. Therefore, the subsequent electrochemical measurement is performed in the narrow voltage window.

The rate capability of Na_{0.67}MnO₂ and Na_{0.67}Fe_{0.20}Ni_{0.15}Mn_{0.65}O₂ was performed at various current densities ranging from 0.1C to 2.0C in the narrow voltage window (2.0 V to 3.8 V). The initial capacity of Na_{0.67}MnO₂ at 0.1C is ~160 mA h g⁻¹, while the reversible capacity decreases to 115 mA h g⁻¹ at the current density of 2.0C as shown in Fig. 3a. After the current density reduces back to 0.1C, the reversible capacity recovers to ~160 mA h g⁻¹ immediately. After the rate capability test, the cell was further cycled at 1.0C to evaluate its long-term cycling stability. As shown in Fig. 3b, the reversible capacity of Na_{0.67}MnO₂ remains at 134 mA h g⁻¹ after 225 cycles, corresponding to a low capacity decay rate of 0.01% per cycle. The coulombic efficiency remains ~100% during the long-term cycling, indicating the excellent reversibility of the Na-ion insertion/extraction reaction. An exceptional battery

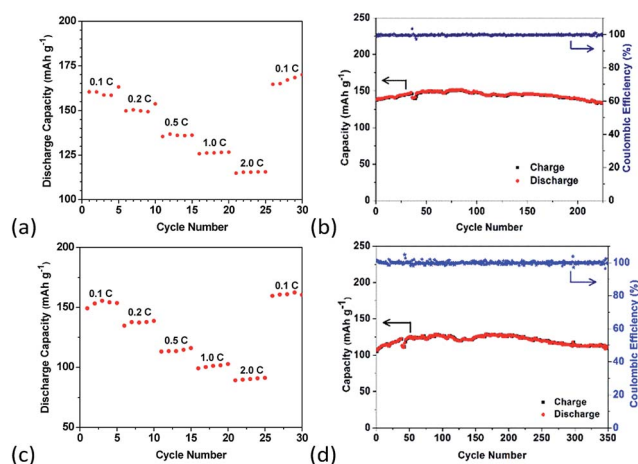


Fig. 3 (a) Rate capability of Na_{0.67}MnO₂; (b) capacity retention of Na_{0.67}MnO₂ cycled at a rate of 1.0C after the rate test; (c) rate capability of Na_{0.67}Fe_{0.20}Ni_{0.15}Mn_{0.65}O₂; (d) capacity retention of Na_{0.67}Fe_{0.20}Ni_{0.15}Mn_{0.65}O₂ cycled at a rate of 1.0C after the rate test.

performance is also observed for the Na_{0.67}Fe_{0.20}Ni_{0.15}Mn_{0.65}O₂ cathode. The initial capacity of Na_{0.67}Fe_{0.20}Ni_{0.15}Mn_{0.65}O₂ at 0.1C is ~150 mA h g⁻¹, while the reversible capacity decreases to 90 mA h g⁻¹ at the current density of 2.0C as shown in Fig. 3c. After the current density reduces back to 0.1C, the reversible capacity recovers to ~150 mA h g⁻¹ immediately. After the rate capability test, the current density increases to 1.0C to evaluate the long-term cycling stability. As shown in Fig. 3d, the reversible capacity of Na_{0.67}Fe_{0.20}Ni_{0.15}Mn_{0.65}O₂ remains at 115 mA h g⁻¹ after 350 cycles with negligible capacity decay. The coulombic efficiency remains ~100% during the long-term cycling, demonstrating the high efficiency of Na-ion insertion/extraction. The long-term cycling stability of Na_{0.67}MnO₂ and Na_{0.67}Fe_{0.20}Ni_{0.15}Mn_{0.65}O₂ after the rate test is compared in Fig. 4. It can be observed that the initial capacity of Na_{0.67}MnO₂ at 1.0C is higher than that of Na_{0.67}Fe_{0.20}Ni_{0.15}Mn_{0.65}O₂. However, the reversible capacity of Na_{0.67}Fe_{0.20}Ni_{0.15}Mn_{0.65}O₂ is higher than that of Na_{0.67}MnO₂ after 350 cycles. The reversible capacity of Na_{0.67}MnO₂ decreases to 15 mA h g⁻¹ after 800 cycles, while the reversible capacity of Na_{0.67}Fe_{0.20}Ni_{0.15}Mn_{0.65}O₂ remains at 80 mA h g⁻¹ after 900 cycles. The long-term cycling stability demonstrated that iron and nickel doped sodium metal oxide exhibits much better cycle life than Na_{0.67}MnO₂. The nickel doping enhances the cycling stability by

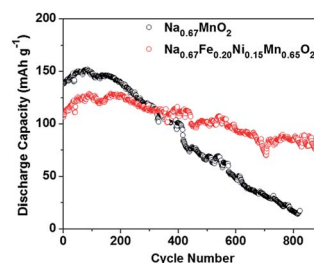


Fig. 4 Capacity retention of Na_{0.67}MnO₂ and Na_{0.67}Fe_{0.20}Ni_{0.15}Mn_{0.65}O₂ cycled from 2.0 V to 3.8 V at a rate of 1.0C after the rate test.

alleviating the volume change and disproportionation of Mn^{3+} , but reduces the reversible capacity. Partially substituting nickel with iron can maintain the high cycling stability and increase the reversible capacity. Therefore, the superior rate capability and long-term cycling stability demonstrate that $\text{Na}_{0.67}\text{Fe}_{0.20}\text{Ni}_{0.15}\text{Mn}_{0.65}\text{O}_2$ is a promising cathode material for advanced Na-ion batteries.

The mechanism for poor cycle life in the expanded voltage window of P2-type layered sodium metal oxides was investigated using XRD. To measure XRD, the $\text{Na}_{0.67}\text{MnO}_2$ electrodes were pre-cycled in a coin cell in the narrow voltage window (2.0 V to 3.8 V), and then fully charged to 3.8 V and maintained at 3.8 V for 24 hours. After that, the cell was disassembled, and the $\text{Na}_{0.67}\text{MnO}_2$ cathode was immersed in dimethyl carbonate to remove the NaClO_4 salt, and then dried in a vacuum oven. As shown in Fig. 5a, the XRD pattern for $\text{Na}_{0.67}\text{MnO}_2$ is well maintained after the 1st charge and 20 cycles, demonstrating excellent structural stability in the narrow cutoff window. For comparison, the XRD patterns for electrodes that were cycled after the 1st charge and 20 cycles in an expanded voltage window (1.5 V to 4.3 V) are also measured at 2.7 V and 4.3 V to investigate the structural change in the expanded cutoff window. As shown in Fig. 5b, the XRD peaks for $\text{Na}_{0.67}\text{MnO}_2$ become weaker and two new peaks at lower degrees (12° and 26°) appear at 4.3 V, demonstrating the formation of a new crystal phase due to the oxidation of Mn^{3+} to Mn^{4+} . The negative shift of XRD peaks demonstrates that the new phase has a larger layer distance. The volume expansion and shrinkage upon cycling favor the dissolution of Mn^{2+} . After the electrode is discharged to 2.7 V (Fig. 5c), which is the open circuit potential of sodium ion batteries, the crystal structure of $\text{Na}_{0.67}\text{MnO}_2$ can be recovered, indicating a good structural reversibility during

the sodiation/desodiation process in the expanded cutoff window. Although the structural change is still reversible when the electrode is cycled in an expanded window, the new phase formation with a large volume change may accelerate the capacity decay.

In addition, the dissolution of Mn^{2+} after cycling in an expanded voltage window is also observed by high resolution TEM images in Fig. 6. The pristine $\text{Na}_{0.67}\text{MnO}_2$ particle (Fig. 6a) and the particle at 3.8 V (Fig. 6b) after 30 cycles exhibit a similar layered structure, demonstrating that negligible structural changes or Mn^{2+} dissolution occur in the narrow cutoff window, while an obvious corrosion area can be observed in the particle at 4.3 V (Fig. 6c) after 30 cycles, indicating that severe Mn^{2+} dissolution takes place in the expanded cutoff window. Furthermore, obvious cracks (Fig. 6d) are formed after cycling at the expanded cutoff window for 30 cycles due to the volume expansion during the sodiation/desodiation process, which facilitates the dissolution of Mn^{2+} . Therefore, the XRD and high resolution TEM results confirm that the volume expansion and disproportionation of Mn^{3+} are the main reasons for capacity decay of the $\text{Na}_{0.67}\text{MnO}_2$ electrode.

To improve the performance of P2-type sodium metal oxides in the expanded voltage window, an ALD method is employed to deposit a thin layer (5 nm) of Al_2O_3 on the $\text{Na}_{0.67}\text{MnO}_2$ electrode to accommodate the volume change and mitigate the dissolution of Mn^{2+} in the electrolyte. A thin layer (5 nm) of Al_2O_3 is conformally coated on the surface of $\text{Na}_{0.67}\text{MnO}_2$ particles as demonstrated in the high resolution TEM image (Fig. S9†). As shown in Fig. 7a, the Al_2O_3 coated $\text{Na}_{0.67}\text{MnO}_2$ electrode shows similar charge/discharge curves in the expanded voltage window as the pristine electrode in Fig. 2c, demonstrating that Al_2O_3 coating does not influence the reaction between $\text{Na}_{0.67}\text{MnO}_2$ and sodium ions. In Fig. 7b, an initial capacity of 150 mA h g^{-1} is achieved, and a reversible capacity of 129 mA h g^{-1} can be maintained for 100 cycles at a current density of 0.1C, corresponding to a slow capacity decline rate of 0.14% per cycle. The lower capacity of the Al_2O_3 coated $\text{Na}_{0.67}\text{MnO}_2$ electrode than the bare $\text{Na}_{0.67}\text{MnO}_2$ electrode is

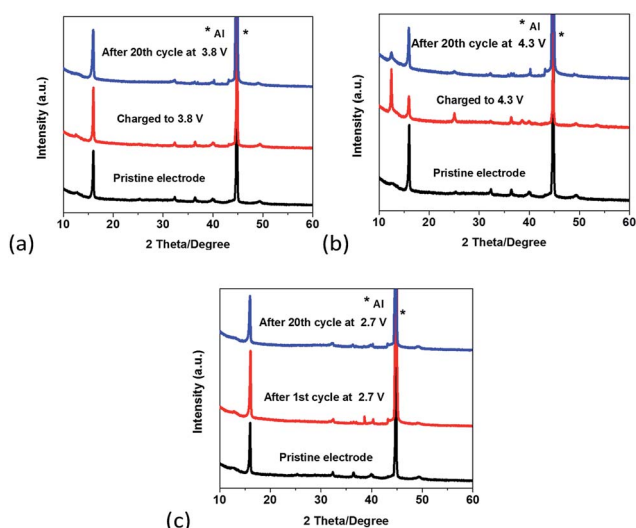


Fig. 5 (a) XRD patterns of the pristine $\text{Na}_{0.67}\text{MnO}_2$ electrode, $\text{Na}_{0.67}\text{MnO}_2$ electrode charged to 3.8 V and $\text{Na}_{0.67}\text{MnO}_2$ electrode at 3.8 V after 20 cycles; (b) XRD patterns of the pristine $\text{Na}_{0.67}\text{MnO}_2$ electrode, $\text{Na}_{0.67}\text{MnO}_2$ electrode charged to 4.3 V and $\text{Na}_{0.67}\text{MnO}_2$ electrode at 4.3 V after 20 cycles; (c) XRD patterns of the pristine $\text{Na}_{0.67}\text{MnO}_2$ electrode, $\text{Na}_{0.67}\text{MnO}_2$ electrode at 2.7 V after the 1st cycle and $\text{Na}_{0.67}\text{MnO}_2$ electrode at 2.7 V after 20 cycles.

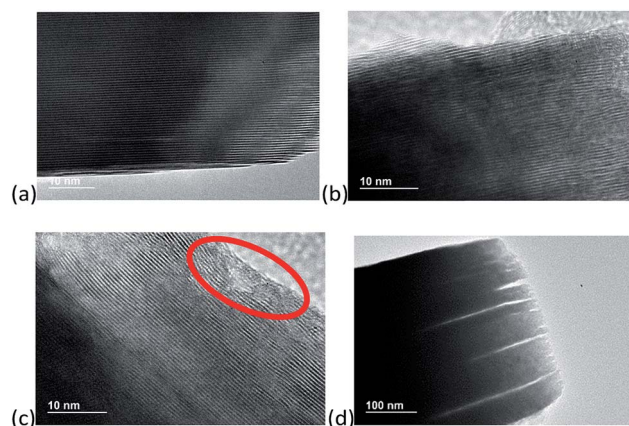


Fig. 6 High resolution TEM images for the fresh $\text{Na}_{0.67}\text{MnO}_2$ electrode (a), and $\text{Na}_{0.67}\text{MnO}_2$ electrodes after 30 cycles with the narrow cutoff window (b) and expanded cutoff window (c and d).

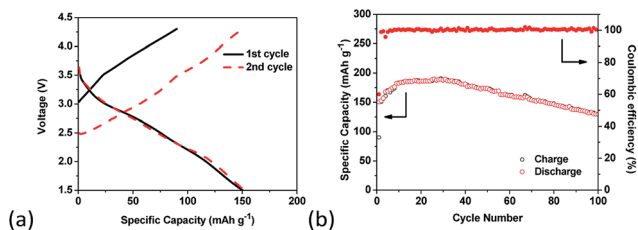


Fig. 7 Galvanostatic charge/discharge curves (a) and capacity retention (b) of the Al_2O_3 coated $\text{Na}_{0.67}\text{MnO}_2$ electrode cycled at a rate of 0.1C in the cutoff window from 1.5 V to 4.3 V.

owing to the worse reaction kinetics. Electrochemical impedance spectroscopy (EIS) was conducted to measure the impedance of Al_2O_3 coated and bare $\text{Na}_{0.67}\text{MnO}_2$ electrodes. As shown in Fig. S10,[†] the depressed semi-circle in the high frequency area represents interphase resistance including coating layer resistance and charge transfer resistance, while the line in the low frequency area stands for ion diffusion resistance. The Al_2O_3 coated $\text{Na}_{0.67}\text{MnO}_2$ electrode exhibits higher interphase resistance than the bare $\text{Na}_{0.67}\text{MnO}_2$ electrode, indicating its slower reaction kinetics. The slower reaction kinetics result in lower reversible capacity during cycling. Though the reversible capacity after Al_2O_3 coating is lower, ALD is an effective method to increase the cycling stability of the $\text{Na}_{0.67}\text{MnO}_2$ cathode in the expanded voltage window. Al_2O_3 coating can effectively accommodate the volume change and mitigate the dissolution of Mn^{2+} .

Conclusions

Three P2-type layered sodium metal oxides were synthesized by a USP method, followed by high temperature treatment. The P2-type $\text{Na}_{0.67}\text{MnO}_2$ slabs exhibit good electrochemical performance in a narrow voltage window, but still suffer from capacity fading in long-term cycling due to the volume change and disproportionation of Mn^{3+} to Mn^{4+} and electrolyte-soluble Mn^{2+} . To mitigate the volume change and dissolution issues, nickel and iron doping was adopted to synthesize P2-type $\text{Na}_{0.67}\text{Ni}_{0.33}\text{Mn}_{0.67}\text{O}_2$ and $\text{Na}_{0.67}\text{Fe}_{0.20}\text{Ni}_{0.15}\text{Mn}_{0.65}\text{O}_2$. $\text{Na}_{0.67}\text{Ni}_{0.33}\text{Mn}_{0.67}\text{O}_2$ exhibits good cycling stability, but much lower capacity than $\text{Na}_{0.67}\text{MnO}_2$. To obtain a high capacity and long cycle life cathode material, Ni is partially substituted by Fe to generate P2-type $\text{Na}_{0.67}\text{Fe}_{0.20}\text{Ni}_{0.15}\text{Mn}_{0.65}\text{O}_2$, which delivers a reversible capacity of 150 mA h g^{-1} at 0.1C. A long-term cycling test demonstrates that the reversible capacity of $\text{Na}_{0.67}\text{Fe}_{0.20}\text{Ni}_{0.15}\text{Mn}_{0.65}\text{O}_2$ at 1.0C remains at 115 mA h g^{-1} after 350 cycles with negligible capacity decay, and the capacity retention is $\sim 70\%$ after 900 cycles, corresponding to a very low capacity decay rate of 0.033% per cycle. To improve the performance of P2-type sodium metal oxides in the expanded voltage window, an ALD method is employed to deposit a thin layer (5 nm) of Al_2O_3 on the $\text{Na}_{0.67}\text{MnO}_2$ electrode to accommodate the volume change and mitigate the dissolution of Mn^{2+} . High cycling stability is achieved for the Al_2O_3 coated $\text{Na}_{0.67}\text{MnO}_2$ electrode, demonstrating that ALD is an effective method to stabilize sodium metal oxide cathodes.

Acknowledgements

We acknowledge the funding support from EVE Energy Co., Ltd. (Sponsor's Num: 14041095) and the support of the Maryland NanoCenter and its NispLab. The NispLab is supported in part by the NSF as a MRSEC Shared Experimental Facility. We thank Prof. Sheryl Ehrman at the University of Maryland, College Park for her technical support.

Notes and references

- B. Dunn, H. Kamath and J. M. Tarascon, *Science*, 2011, **334**, 928–935.
- V. Palomares, P. Serras, I. Villaluenga, K. B. Hueso, J. Carretero-González and T. Rojo, *Energy Environ. Sci.*, 2012, **5**, 5884–5901.
- S. Wenzel, T. Hara, J. Janek and P. Adelhelm, *Energy Environ. Sci.*, 2011, **4**, 3342–3345.
- M. D. Slater, D. Kim, E. Lee and C. S. Johnson, *Adv. Funct. Mater.*, 2013, **23**, 947–958.
- B. L. Ellis and L. F. Nazar, *Curr. Opin. Solid State Mater. Sci.*, 2012, **16**, 168–177.
- E. M. Lotfabad, J. Ding, K. Cui, A. Kohandehghan, W. P. Kalisvaart, M. Hazelton and D. Mitlin, *ACS Nano*, 2014, **8**, 7115–7129.
- D. Su, S. Dou and G. Wang, *Adv. Energy Mater.*, 2015, **5**, 1401205.
- Z. Hu, L. Wang, K. Zhang, J. Wang, F. Cheng, Z. Tao and J. Chen, *Angew. Chem., Int. Ed.*, 2014, **53**, 12794–12798.
- X. Xie, Z. Ao, D. Su, J. Zhang and G. Wang, *Adv. Funct. Mater.*, 2015, **25**, 1393–1403.
- Y. Kim, Y. Park, A. Choi, N. S. Choi, J. Kim, J. Lee, J. H. Ryu, S. M. Oh and K. T. Lee, *Adv. Mater.*, 2013, **25**, 3045–3049.
- J. Qian, X. Wu, Y. Cao, X. Ai and H. Yang, *Angew. Chem., Int. Ed.*, 2013, **52**, 4633–4636.
- C. Woo, J. Kim, S. Park, H. Jo and D. Kim, *Nano Energy*, 2015, **15**, 479–489.
- X. Han, Y. Liu, Z. Jia, Y. C. Chen, J. Wan, N. Weadock, K. J. Gaskell, T. Li and L. Hu, *Nano Lett.*, 2014, **14**, 139–147.
- S. W. Kim, D. H. Seo, X. Ma, G. Ceder and K. Kang, *Adv. Energy Mater.*, 2012, **2**, 710–721.
- J. Billaud, G. Singh, A. R. Armstrong, E. Gonzalo, V. Roddatis, M. Armand, T. Rojo and P. G. Bruce, *Energy Environ. Sci.*, 2014, **7**, 1387–1391.
- M. Guignard, C. Didier, J. Darriet, P. Bordet, E. Elkaïm and C. Delmas, *Nat. Mater.*, 2013, **12**, 74–80.
- R. Berthelot, D. Carlier and C. Delmas, *Nat. Mater.*, 2011, **10**, 74–80.
- N. Yabuuchi, R. Hara, M. Kajiyama, K. Kubota, T. Ishigaki, A. Hoshikawa and S. Komaba, *Adv. Energy Mater.*, 2014, **4**, 1301453.
- Y. H. Jung, A. S. Christiansen, R. E. Johnsen, P. Norby and D. K. Kim, *Adv. Funct. Mater.*, 2015, **25**, 3227–3237.
- N. Sharma, E. Gonzalo, J. C. Pramudita, M. H. Han, H. E. A. Brand, J. N. Hart, W. K. Pang, Z. Guo and T. Rojo, *Adv. Funct. Mater.*, 2015, **25**, 4994–5005.

- 21 R. Qiao, K. Dai, J. Mao, T. C. Weng, D. Sokaras, D. Nordlund, X. Song, V. S. Battaglia, Z. Hussain, G. Liu and W. Yang, *Nano Energy*, 2015, **16**, 186–195.
- 22 Y. Zhu, Y. Xu, Y. Liu, C. Luo and C. Wang, *Nanoscale*, 2013, **5**, 780–787.
- 23 B. L. Ellis, W. R. M. Makahnouk, Y. Makimura, K. Toghill and L. F. Nazar, *Nat. Mater.*, 2007, **6**, 749–753.
- 24 C. Fang, Y. Huang, W. Zhang, J. Han, Z. Deng, Y. Cao and H. Yang, *Adv. Energy Mater.*, 2016, **6**, 1501727.
- 25 P. Barpanda, G. Oyama, S. Nishimura, S. C. Chung and A. Yamada, *Nat. Commun.*, 2014, **5**, 4358.
- 26 C. Luo, Y. Xu, Y. Zhu, Y. Liu, S. Zheng, Y. Liu, A. Langrock and C. Wang, *ACS Nano*, 2013, **7**, 8003–8010.
- 27 C. Luo, J. Wang, L. Suo, J. Mao, X. Fan and C. Wang, *J. Mater. Chem. A*, 2015, **3**, 555–561.
- 28 S. Xin, Y. X. Yin, Y. G. Guo and L. J. Wan, *Adv. Mater.*, 2014, **26**, 1261–1265.
- 29 C. Luo, Y. Zhu, O. Borodin, T. Gao, X. Fan, Y. Xu, K. Xu and C. Wang, *Adv. Funct. Mater.*, 2016, **26**, 745–752.
- 30 Z. Jian, V. Raju, Z. Li, Z. Xing, Y. Hu and X. Ji, *Adv. Funct. Mater.*, 2015, **25**, 5778–5785.
- 31 D. Ma, H. Wang, Y. Li, D. Xu, S. Yuan, X. Huang, X. Zhang and Y. Zhang, *Nano Energy*, 2014, **10**, 295–304.
- 32 W. J. Li, S. L. Chou, J. Z. Wang, J. L. Wang, Q. F. Gu, H. K. Liu and S. X. Dou, *Nano Energy*, 2015, **13**, 200–207.
- 33 H. Kim, Y. U. Park, K. Y. Park, H. D. Lim, J. Hong and K. Kang, *Nano Energy*, 2014, **4**, 97–104.
- 34 Y. N. Zhou, M. Sina, N. Pereira, X. Yu, G. G. Amatucci, X. Q. Yang, F. Cosandey and K. W. Nam, *Adv. Funct. Mater.*, 2015, **25**, 696–703.
- 35 A. Caballero, L. Hernán, J. Morales, L. Sánchez, J. Santos Peña and M. A. G. Aranda, *J. Mater. Chem.*, 2002, **12**, 1142–1147.
- 36 D. Yuan, X. Hu, J. Qian, F. Pei, F. Wu, R. Mao, X. Ai, H. Yang and Y. Cao, *Electrochim. Acta*, 2014, **116**, 300–305.
- 37 J. Cho, T. J. Kim, Y. J. Kim and B. Park, *Chem. Commun.*, 2001, 1074–1075.
- 38 N. Yabuuchi, M. Kajiyama, J. Iwatate, H. Nishikawa, S. Hitomi, R. Okuyama, R. Usui, Y. Yamada and S. Komaba, *Nat. Mater.*, 2012, **11**, 512–517.
- 39 J. Xu, D. H. Lee, R. J. Clément, X. Yu, M. Leskes, A. J. Pell, G. Pintacuda, X. Q. Yang, C. P. Grey and Y. S. Meng, *Chem. Mater.*, 2014, **26**, 1260–1269.
- 40 S. Komaba, N. Yabuuchi, T. Nakayama, A. Ogata, T. Ishikawa and I. Nakai, *Inorg. Chem.*, 2012, **51**, 6211–6220.
- 41 D. Kim, E. Lee, M. Slater, W. Lu, S. Rood and C. S. Johnson, *Electrochem. Commun.*, 2012, **18**, 66–69.
- 42 H. Wang, B. Yang, X. Z. Liao, J. Xu, D. Yang, Y. S. He and Z. F. Ma, *Electrochim. Acta*, 2013, **113**, 200–204.
- 43 B. Mortemard de Boisse, D. Carlier, M. Guignard and C. Delmas, *J. Electrochem. Soc.*, 2013, **160**, A569–A574.